Confidence-Aware 3D Spatial Compounding of 2D Ultrasound Images for Needle Shadow Removal

Hoorieh Mazdarani[1], Rebecca Hibbert[2], James Watterson[3], and Carlos Rossa[1]
[1]*Department of Systems and Computer Engineering, Carleton University, Ottawa, ON, Canada.*
[2]*Department of Radiology, Mayo Clinic, Rochester, MN, United States.*
[3]*Faculty of Medicine, Division of Urology, University of Ottawa, Ottawa, ON, Canada.*

***Abstract*—Ultrasound (US) imaging clarity is often hindered by acoustic shadows caused by highly reflective structures, obscuring critical anatomy in the images. This issue is particularly problematic in needle-based interventions, where needle-induced shadows and reverberations can severely obstruct visualization, complicating the procedure and increasing the risk of misplacement. To address this problem, we propose a new 3D image compounding algorithm to remove needle shadows and allow the US probe to see behind reflective objects. Our approach acquires 2D US images from multiple imaging angles and computes the probability that the US wave has reached each pixel in the images. We then propose a nonlinear function to weight these 2D images based on their pixel intensity and acoustic signal consistency before they are combined to form a 3D volume. Regions corresponding to shadows are adaptively suppressed, while highly informative areas are compounded to create an accurate volumetric representation. This volume is then sliced along arbitrary imaging planes to form new, shadow-free images.**

Experimental validation in phantom tissue comparing the original US images with the images created with the proposed algorithm shows significant improvement in image clarity and tissue inclusion delineation. The proposed method is compared against other conventional image compounding techniques and shows improvements in image signal to noise ratio and normalized cross corelation. By enhancing the reliability of 3D US image compounding, the proposed multivariable, nonlinear weighting function contributes to more precise and accurate US image guidance for needle-based diagnostics and interventions.

***Index Terms*—Ultrasound imaging, 3D compounding, shadow removal, needle imaging**

I. INTRODUCTION

Ultrasound (US) is a widely used imaging modality to guide targeted percutaneous surgery due to its real-time imaging capability, cost-effectiveness, and accessibility. These procedures involve inserting a needle or catheter into a target within the body under US guidance, and are commonly employed in interventions such as tumour ablation, biopsy, and nephrolithotomy [1]. Despite its advantages, US imaging presents significant challenges for precise needle targeting. US imaging is inherently limited by acoustic shadows caused by highly reflective structures, such as bones, air pockets, and the surgical tools themselves, which obscure critical anatomical structures in the images, compromising accurate needle placement [2]. This issue becomes even more problematic in interventions involving multiple needles, such as kidney tumour ablation, where overlapping shadows and reverberations caused by ablation probes can obstruct the target area in the image, complicating the procedure and increasing the risk of misplacement.

Various techniques have been developed to enhance visualization and needle targeting, and address the challenges posed by needle shadowing and low image quality. Needle shadow removal methods range from advanced image processing, such as model-based shadow detection and deep learning denoising, to compounding approaches that integrate US beam steering to enhance clarity [3]–[10]. In most of these applications, shadow detection is task-specific and mainly based on heuristic image features or special anatomical constraints. With the help of deep learning, these algorithms can detect and distinguish shadows originating from different sources [11], [12]. However, they require a large amount of data for training.

One common shadow removal approach is 2D image compounding, in which images are acquired from multiple beam steering directions without physically moving the probe. The images obtained from different steering directions are then merged into a single compound image [13]. While this approach can partially reduce needle shadows, it is limited by the inherent constraints and limited angle of 2D beam steering, and therefore, it may not completely eliminate shadowing artifacts depending on the needle position and angle relative to the probe. A more effective solution is 3D spatial compounding, where multiple images are acquired by orienting the ultrasound probe to capture images from different perspectives [14]. The images are then combined to fill in shadowed areas with valid data. To combine images acquired from different angles, [15] developed a method that assigns regional weights to pixels depending on the local incidence angle of the ultrasound beam. Another method uses multiscale information to weigh the contributions of each image in the final compounded image [16]. In [17], image features are used to remove outlier pixels due to artifacts and down weigh inconsistent regions.

While traditional 3D compounding methods improve shadow removal and image quality compared to 2D beam steering [18], they cannot tell apart regular image data from shadows, often resulting in missing or distorted anatomical structures. In particular, they tend to retain high intensity pixels, which may arise from unwanted reverberations in

---

Email: hooriehmazdarani@cmail.carleton.ca; rossa@sce.carleton.ca

We acknowledge the support of the Natural Sciences and Engineering Research Council of Canada (NSERC), [funding reference number ALLRP 580714-22]. Cette recherche a été financée par le Conseil de recherches en sciences naturelles et en génie du Canada (CRSNG), [no. de référ. 580714-22].

the image. To minimize this problem, probabilistic methods capable of distinguishing between regular data and shadows may be considered to weigh the contribution of each image in the final compounded image. In [19], a support vector machine generates probabilistic maps to detect shadows in each image before combining them. An evolution of this method, presented in [20], uses a convolution neural network to estimate the structure's echogenicity and weight each image accordingly. These approaches require large labelled datasets for training. To address this limitation, multi-scale image fusion using Laplacian pyramids can be tuned to retain the most prominent image features and reject outlier pixels [21].

Alternatively, confidence maps may be used to assess image quality. A confidence map is derived from intensity variations and acoustic signal consistency to differentiate between high-certainty and low-certainty regions in an image. Karamalis *et al.* introduced the concept in 2012 [22], and ever since, confidence maps have been widely used in US image processing for quality assessment [23], [24]. It has also been applied to 3D image compounding to deal with uncertainties in attenuated regions [25], where confidence values become a weight parameter to compose several image clusters.

The works mentioned above focus primarily on enhancing image quality from multiple projections; however, they are designed for tissue imaging and speckle noise reduction rather than needle shadow removal. Recovering shadowed areas in an image occluded by the needle shaft remains an open and critical problem in US-guided percutaneous surgery [26], [27].

In this paper, we present a new approach specifically designed to minimize needle shadows in US images. Similar to 3D image compounding, we acquire overlapping 2D images from different angles to bypass highly reflective needles and capture echoes from regions otherwise obscured by them. We then measure the confidence of every pixel in each 2D image based on the probability that the US beam has reached that point in the tissue in the presence of the needle. Unlike previous methods, before these angled scans are combined into a volume through a function-based compounding method, we propose to assign weights to every pixel in overleaping images based on both US pixels' intensity and confidence values. These weighting function, specifically designed to minimize needle shadowing, emphasizes the anatomical structures and the needle, while surpassing shadowed areas and allowing the algorithm to see around attenuating or reflective structures and fill in these shadowed areas with valid data.

Previously reported methods cannot distinguish high intensity pixels arising from needle reverberations from those arising from anatomical structures. As a result, they would remove the needle from the image. In contrast, as the proposed method merges confidence maps with pixel intensity in a unified weighting function, we show that our method improves anatomical clarity and contrast in reconstructed images, while preserving the needle in the image, which is essential for real-time guidance. The next section introduces the confidence-aware 3D compounding algorithm and the novel weighting function. We validate our approach experimentally in Sec. III on artificial phantoms imaged by a linear US probe, and compare its performance against two conventional 3D compounding techniques in Sec. IV. The results demonstrate that our method effectively reduces shadow areas in the image and enhances image quality. The results are followed by a discussion and conclusion on the proposed contribution and recommendations. This advancement holds potential for improving imaging in interventional procedures, robotic surgery, and diagnostic assessments.

II. CONFIDENCE-AWARE IMAGE COMPOUNDING

The proposed 3D compounding algorithm involves 5 steps:

1) A 3D, empty voxel $\mathbf{V}$ is created. Each pixel in the voxel will be filled in with pixels from 2D US images.
2) 2D US images of a sample are acquired from different angles. The operator physically orients the US probe to image the target area from slightly different angles while the probe's position and orientation are measured in real-time. The image's corresponding position in the voxels is then determined through a rigid spatial transformation.
3) A physics-based model calculates the probability that the acoustic wave has reached a certain area in each 2D image, indicating the reliability of every image pixel;
4) The pixels from each image are weighted by a non-linear function of pixel intensity and confidence value. The overleaping pixels are passed through a weighted averaging before they fill in the 3D voxel;
5) The voxel is sliced along an arbitrary imaging plane to form new, shadow-free 2D images.

These steps are explained in detail in the next subsections. Hereafter, bold lower and upper case letters stand for vectors and matrices, respectively, and unbolded letters for scalars.

A. Multi-angle Image Acquisition and Registration

Assume a sequence of 2D US images of a tissue sample acquired from different orientations while the 3D position and orientation of the probe are recorded. A series of coordinate frames must be defined to find the rigid transformation relating the position of each pixel in the US image to the corresponding voxel in 3D volume. To that end, let (${}^{\mathtt{W}}\mathcal{F}$) be the world reference frame, and (${}^{\mathtt{S}}\mathcal{F}$) the coordinate frame describing the position and orientation of the sensor attached to the US probe. Further, let (${}^{\mathtt{P}}\mathcal{F}$) be the coordinate frame of the US imaging plane, and (${}^{\mathtt{V}}\mathcal{F}$) the reference frame given the origin of the 3D volume $\mathbf{V}$. The homogeneous transformation ${}^{\mathtt{V}}\mathbf{T}_{\mathtt{P}}$ from the probe frame ${}^{\mathtt{P}}\mathcal{F}$ to the 3D volume frame ${}^{\mathtt{V}}\mathcal{F}$ is:

$$
{}^{\mathtt{V}}\mathbf{T}_{\mathtt{P}} = {}^{\mathtt{V}}\mathbf{T}_{\mathtt{W}}\ {}^{\mathtt{W}}\mathbf{T}_{\mathtt{S}}\ {}^{\mathtt{S}}\mathbf{T}_{\mathtt{P}} \tag{1}
$$

where ${}^{\mathtt{B}}\mathbf{T}_{\mathtt{A}}$ is the homogeneous transformation from ${}^{\mathtt{A}}\mathcal{F}$ to ${}^{\mathtt{B}}\mathcal{F}$.

Now, let each 2D image $\mathbf{S}$ have pixels with intensity $I(\mathbf{p})$ where $\mathbf{p} = [m\ n\ 0]^T$ gives the coordinate of the pixel in image $\mathbf{S}$ and m and n are the vertical and horizontal pixel coordinates in the image. The equivalent location of each pixel in the 3D volume $\mathbf{V}$ is:

$$
\mathbf{x} = {}^{\mathtt{V}}\mathbf{T}_{\mathtt{P}}(\mathbf{p}). \tag{2}
$$

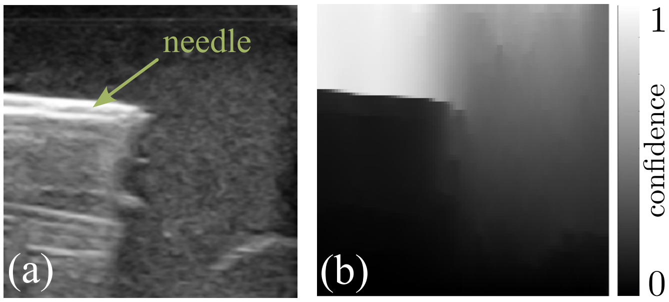

Fig. 1. Longitudinal US image of an 18-G needle imaged from the top of the image. (a) show the reverberations caused by the needle and (b) the corresponding confidence map. The confidence below the needle is zero.

where each position $\mathbf{x} \in \mathbf{V}$ is hereafter called a voxel. To convert the coordinates of the pixel to voxel, the nearest neighbour is applied to the result of (2) and find the nearest voxel in the 3D volume [14].

In traditional image compounding, pixels that overlap onto a single voxel are averaged and then added to the 3D volume. The intensity of voxel $I(\mathbf{x})$ is:

$$I(\mathbf{x}) = \frac{1}{N} \sum_{N} I(\mathbf{p}) \tag{3}$$

where N is the number of overlapping pixels. This formulation weighs all images equally. To remove the effect of artifacts and shadows, this equation must be reformulated to account for the acoustic signal quality of each pixel.

B. US Confidence Map

As acoustic waves travel through tissue, they experience acoustic attenuation and reflections. The intensity of the echoes that return to the probe are converted into pixel intensity in a 2D image. Consequently, the signal quality is often non-uniform across the image. Confidence maps, introduced in [22], evaluate the probability that the acoustic wave has reached the point in the tissue corresponding to an image pixel.

Considering the confidence value of each pixel is $C(\mathbf{p}) \in [0 \quad 1]$. For pixels near the US probe $C(\mathbf{p}) \to 1$ (the highest probability that the US wave has reached those points), while for those located at the bottom of the image $C(\mathbf{p}) \to 0$. For other pixels in between, the probability is unknown and must be calculated using an US propagation model. The algorithm used in this work is briefly provided here, while the complete method can be found in [22]. It involves the following steps:

1) Calculate the US propagation weight w_{ij} between two adjacent pixels $\mathbf{p}_i$ and $\mathbf{p}_j$ as:

$$w_{ij} = \begin{cases} e^{-\beta|g_i - g_j|} & \text{vertically adjacent} \\ e^{-\beta(|g_i - g_j| + \gamma)} & \text{horizontally adjacent} \\ e^{-\beta(|g_i - g_j| + \sqrt{2}\gamma)} & \text{diagonally adjacent} \end{cases} \tag{4}$$

where g is the attenuated signal intensity at each pixel with depth d and intensity $I(\mathbf{p})$, defined as $g = I(\mathbf{p})e^{-\alpha d}$. Here, α, β, and γ are tunable attenuation coefficients.

2) Calculate the Laplacian matrix $\mathbf{L}$ as:

$$\mathbf{L}_{ij} = \begin{cases} \sum_j w_{ij} & i = j \\ -w_{ij} & \text{adjacent pixels} \\ 0 & \text{otherwise} \end{cases} \tag{5}$$

3) Rearrange $\mathbf{L}$ according to the weight between all known pixels $\mathbf{L}_K$ and the weight between all unknown pixels $\mathbf{L}_U$ as:

$$\mathbf{L} = \begin{bmatrix} \mathbf{L}_K & \mathbf{B} \\ \mathbf{B}^T & \mathbf{L}_U \end{bmatrix} \tag{6}$$

4) Solve the following linear equation for the unknown confidence vector $\mathbf{c}_U$ based on the known confidence vector $\mathbf{c}_K$:

$$\mathbf{L}_U \; \mathbf{c}_U = -\mathbf{B}^T \; \mathbf{c}_K \tag{7}$$

5) Finally, the confidence map is formed by accumulating $\mathbf{c}_N$ and $\mathbf{c}_U$ in matrix $\mathbf{C}$.

The confidence of each pixel depends on the tissue properties and also on the path travelled by the signal from that point. Therefore, as a strongly reflective object blocks the ultrasound signal propagation, it decreases the confidence level of pixels beneath it. This is highly beneficial in detecting shadowed regions or reverberations below such reflective objects, like a needle, as can be seen in Fig. 1.

C. Confidence-Aware 3D Compounding

Once the confidence value of every pixel in each 2D image is known, overlapping pixels must be weighted or averaged to fill in the corresponding 3D voxel. While confidence-based weighted averaging for 3D compounding was discussed in [25] with improvements in image quality, previous works do not consider the presence of the needle in the image. As shown in Fig. 1, the confidence level of the needle and anything below it in the image tends to zero. If the algorithm only considers the pixel confidence when forming the 3D volume, such as the formulation in (3), the needle will be invisible in the reconstructed 3D volume. Conversely, if only the pixel intensity is used, the high intensity pixels below the needle shaft caused by reverberation will shadow the tissue.

To solve this problem, we propose a nonlinear weighting function that takes into account both the confidence $C(\mathbf{p})$ at $\mathbf{p}$ and the intensity $I(\mathbf{p})$ of each pixel. Let the intensity of the compounded voxel $\mathbf{x}$ in the 3D volume, first introduced in (3), be redefined with a normalized weighted sum instead:

$$I(\mathbf{x}) = \frac{\sum_N f(C(\mathbf{p}), I(\mathbf{p})) \times I(\mathbf{p})}{\sum_N f(C(\mathbf{p}), I(\mathbf{p}))}, \tag{8}$$

where $f(C, I)$ is a function to be defined that depends on both $C(\mathbf{p})$ and $I(\mathbf{p})$. We observe that different combinations of $C(\mathbf{p})$ and $I(\mathbf{p})$ indicate specific elements in an image:

- High $I(\mathbf{p})$ and high $C(\mathbf{p})$ indicate anatomical structures with informative data. As these areas must be retained with emphasis, the function should output $f(C, I) \to 1$;
- High $I(\mathbf{p})$ and low $C(\mathbf{p})$ indicate a highly reflective object, such as a needle, which must be kept, therefore the weight function should output $0 << f(C, I) < 1$;

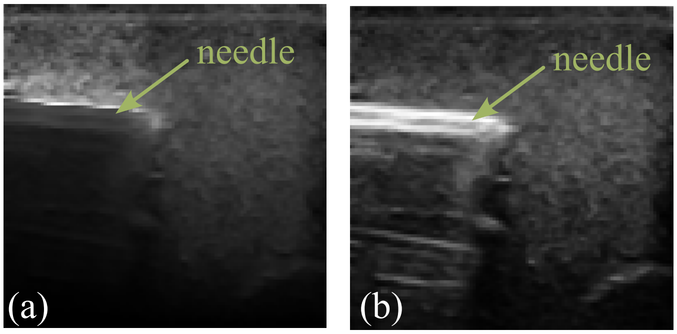

Fig. 2. Comparison between confidence-based weighting and the proposed weighting in (9), of the US image and confidence from Fig. 1. In (*a*) multiplying pixels' intensity by their confidence map suppresses the needle. In (*b*) multiplying pixels' intensity by (9) results in a clear image of the needle while its reverberations are eliminated.

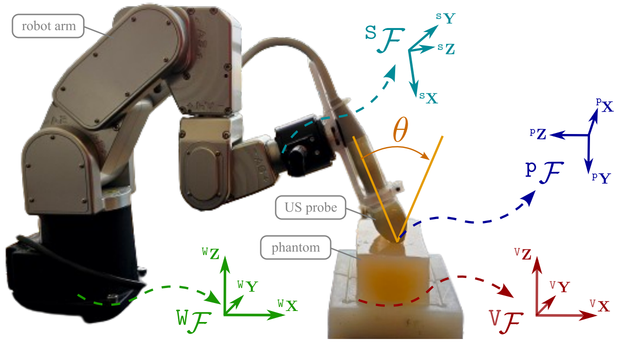

Fig. 3. Image acquisition setup with a linear US probe. Coordinates frames defined for the US imaging plane, position sensor, world frame, and the 3D volume are ${}^{P}\mathcal{F}$, ${}^{S}\mathcal{F}$, ${}^{W}\mathcal{F}$, and ${}^{V}\mathcal{F}$ respectively.

- Low $I(\mathbf{p})$ and high $C(\mathbf{p})$ corresponds to tissue above an attenuating object, which higher $I(\mathbf{p})$ than regular tissue, therefore the function should output $0 < f(C, I) << 1$;
- Low $I(\mathbf{p})$ and low $C(\mathbf{p})$ indicate a shadowed area with invalid data. As it should be suppressed from the image, the desired weight is $f(C, I) \rightarrow 0$.

Given the desired behaviour of $f(C, I)$ for different ranges of $I(\mathbf{p})$ and $C(\mathbf{p})$, $f(C, I)$ may be defined as:

$$f(C, I) = \frac{1}{1 + e^{-[k_1 C(\mathbf{p}) + k_2 I(\mathbf{p}) - k_3]}}, \tag{9}$$

where k_1, k_2, and k_3 are tunable constants that can be chosen to satisfy the above requirements.

Fig. 2(a) shows the result of multiplying the US image from Fig. 1(a) by its confidence map (shown in Fig. 1(b)). Fig. 2(b) shows the result of multiplying every pixel from Fig. 1(a) by (9) for $k_1 = 5$, $k_2 = 10$, and $k_3 = 6$. With the proposed formulation, the needle and surrounding tissue are given a higher weight, while keeping the weight of the shadowed low. This will ensure that the needle is visible in the reconstructed volume and the influence of shadowed areas is negligible.

TABLE I
ULTRASOUND IMAGE ACQUISITION PARAMETERS

frequency	gain	focus	depth	dyn. range	power
7.5 MHz	85 %	14-21 mm	40 mm	102 dB	−2 dB

III. EXPERIMENTAL VALIDATION AND RESULTS

While the proposed algorithm works with freehand ultrasound, to simplify the experimental validation and ensure consistency across different trials, we use the robotic-actuated setup shown in Fig. 3. A 40-mm linear US probe (L15-7H40-A5 from Telemed Ultrasound, Vilnius, Lithuania) is attached to the end-effector of a 6-DOF robot arm (Meca500 from Mecademic, Montréal, Canada). The US machine streams images at 30 Hz according to the parameters given in Table I.

The US probe is positioned on top of two different artificial phantoms made of 4% agar. Harder, small tumour-like inclusions made of 10% agar are inserted at different spots in each phantom. With the phantoms fixed in place, the US probe is oriented at 5 different angles about ${}^{P}x$, i.e., $\theta = -20°, -10°, 0°, 10°, 20°$. At each of these orientations, the robot slides the probe along ${}^{P}z$ by 20 mm with increments of 0.1 mm while US images are taken. The process above is repeated for all orientations. After all 5 sets of scans are taken, an 18-G needle is inserted in the phantom longitudinally to the imaging plane. The image acquisition process is then repeated with the needle in the tissue. Once the images are acquired, the 3D volume is created following the procedure outlined earlier. The volume can then be sliced along any imaging plane to produce new 2D images that can be compared with their real, corresponding images taken at the same location and orientation.

In the first test scenario, the phantom contains one inclusion, as it can be seen in the single US image in Fig. 4(a), taken at $\theta = 0$ before the needle is inserted. Fig. 4(b), taken at the same location with the needle inserted, shows that when the needle is aligned to the imaging plane, it degrades the image quality as it blocks the US signal and shadows the anatomical structure beneath it. The volumetric image of the tissue reconstructed with the proposed algorithm is shown in Fig. 4(c). This volume is then sliced along the orientation and about the same position as that of Fig. 4(b). The resulting image in Fig. 4(d) shows a higher quality and better delineation of the inclusion below the needle than the original 2D image.

In the second test scenario, we used the same phantom but inserted the needle from a different insertion point toward the inclusion. Fig. 4(e) Fig. 4(f) show the original 2D image and the one created with the proposed method. These results show the ability of the proposed method in reconstructing the volume and recovering the shadowed area. The 3D volume can be seen in Fig. 4(g-h).

In the third scenario, the phantom contains three smaller inclusions, as shown in the original 2D image in Fig. 5(a). Once the needle is inserted, the shadowing effect is again visible, see Fig. 5(b). The same procedure as the first two

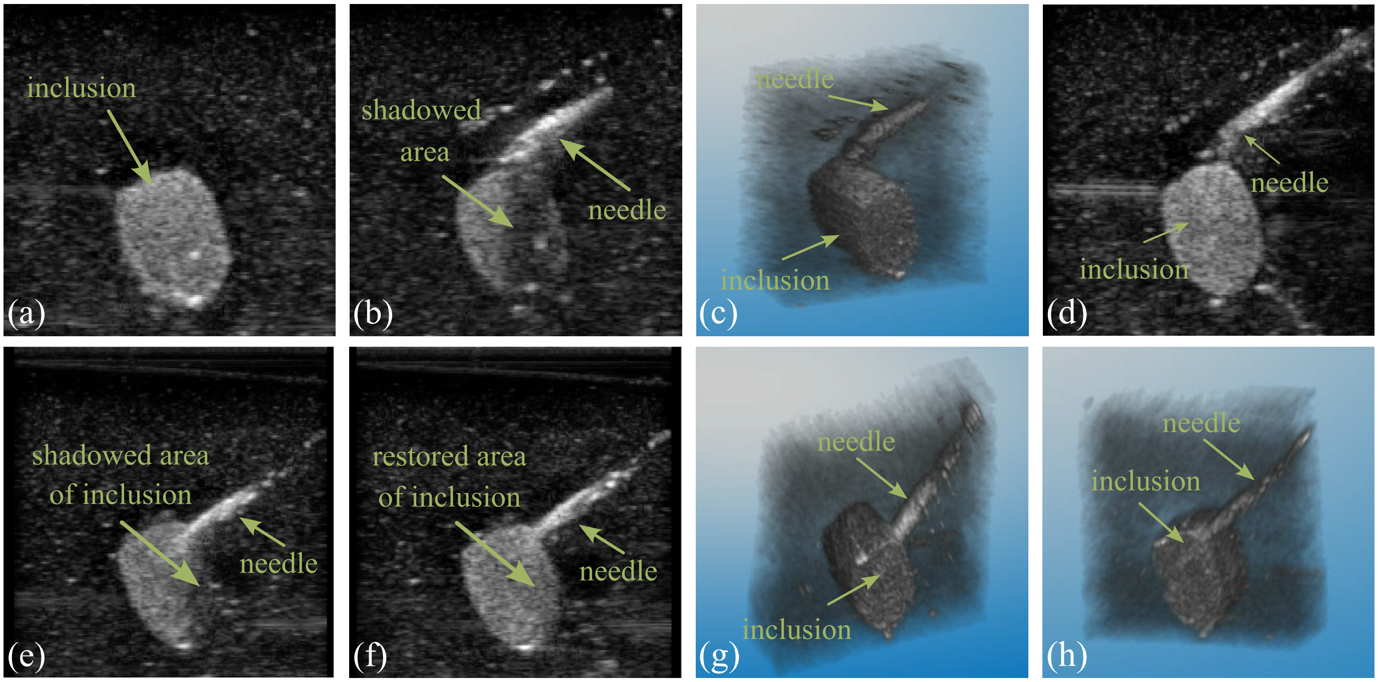

Fig. 4. Experimental results in Scenarios 1 (b-d) and 2 (e-h). In (a) the US image of the phantom containing an inclusion, used in both Scenarios. Fig. (b) shows how the presence of the needle darkened the inclusion. (c) shows the reconstructed 3D volume compounded from multi-angle scans, and (d) the resampled image taken at the same location as that in (b). In (e) the image shows the shadowed area of the inclusion caused by the needle in scenario 2, (f) shows a resampled slice at the same location as in (e) acquired from the compounded volume shown in (g) and (h).

scenarios is followed for image reconstruction. The volume is seen in Fig. 5(c), and the corresponding image taken from the volume along the same orientation as Fig. 5(b) is shown in Fig. 5(d). As we can see again, the reconstructed image provides better detail and better inclusion delineation than the original single image.

IV. COMPARISON

To quantitatively evaluate the proposed method, we compare our results against two similar algorithms. The first one is the standard 3D compounding, where the contribution of overlapping pixels to a single voxel is averaged [14]. The second method is the confidence-weighted averaging presented in [25]. To measure the quality of the images, signal-to-noise ratio (SNR) and normalized cross-correlation (NCC) are computed for a region of interest (ROI) in the original and reconstructed images containing the inclusion. SNR quantifies the level of information (signal) relative to unwanted image distortions (noise), as a metric to assess image clarity as:

$$SNR = \frac{\mu_{ROI}}{\sigma_{\mathrm{B}}},$$

where $\mu_{\mathtt{ROI}}$ is the mean of the inclusion area and σ_{B} is the standard deviation of the background. The higher the SNR, the clearer and more detailed the image is. NCC measures the alignment of intensity between two images while being invariant to changes in brightness. It can be defined as:

$$NCC = \frac{\sum_{\mathbf{p}}(I_{ROI}(\mathbf{p}) - \bar{I}_{ROI})(T_{ROI}(\mathbf{p}) - \bar{T}_{ROI})}{\sqrt{\sum_{\mathbf{p}}(I_{ROI}(\mathbf{p}) - \bar{I}_{ROI})^2 \sum_{\mathbf{p}}(T_{ROI}(\mathbf{p}) - \bar{T}_{ROI})^2}},$$

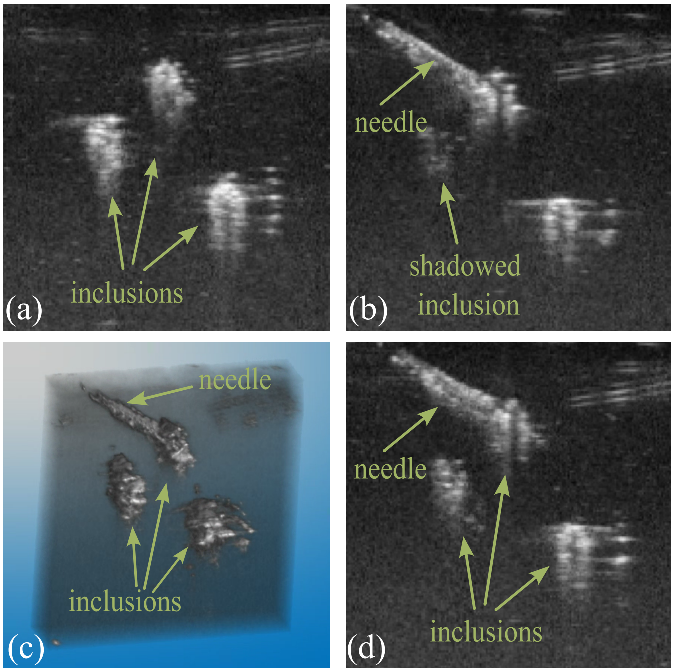

Fig. 5. Experimental results in Scenarios 3: In (a) the US image of the phantom containing three inclusions. Fig. (b) shows how the needle has darkens one of the inclusions. In (c) the 3D volume compounded from multi-angle scans is shown, from which the resampled image shown in (d) is taken, at the same location as that of (b).

TABLE II
COMPARISON OF SNR AND NCC IN THE ROI WITH OTHER ALGORITHMS

	Averaging [15]		CW-weight [25]		Proposed method	
Test scenario	SNR	NCC	SNR	NCC	SNR	NCC
Scenario 1	8.15	0.69	8.21	0.88	**8.27**	**0.95**
Scenario 2	8.13	0.71	8.25	0.92	**8.33**	**0.94**
Scenario 3	7.67	0.74	8.26	0.90	**8.38**	**0.92**

where I_{ROI} and $\bar{I}_{ROI}$ are the ROI of the reconstructed image and the mean pixel intensity within, respectively, and T_{ROI} and $\bar{T}_{ROI}$ are the ROI of the ground truth slice, like Fig. 4(a), and the mean pixel intensity within. If $T_{ROI} = I_{ROI}$, then $NCC = 1$. The results provided in Table II demonstrate the superior ability of the proposed method to fill the shadowed regions and enhance the image quality.

V. CONCLUSION AND FUTURE WORK

In this paper, we presented a confidence-aware US image compounding algorithm to address problems related to needle shadowing artifacts that cover sensitive structures in the image. We proposed a two-variable weighting function to be used in a normalized weighted voxel averaging. This function is capable of removing low-confidence areas, containing the shadows and other artifacts, while retaining informative structures. The experimental validation performed on artificial models shows that the algorithm can successfully generate an enhanced 3D volume by retaining information from sensitive structure and removing shading artifacts. A comparison of the obtained results with the two similar methods shows that the proposed algorithm offers superior image quality and lesion delineation than standard methods.

In the experimental results, we used a robotic actuated US probe to obtain and compare images taken at the same position and orientation. Yet, free-hand imaging will be more applicable in real surgical procedures. Therefore, in the next step, we will focus on integrating machine learning approaches for sensorless image registration. In addition, while we tried to minimize the calculation complexity of the method, image reconstruction takes about 2 minutes and is performed offline. Another focus of future work will be on implementing this method in real-time. Finally, validating the method on ex-vivo tissue to achieve more realistic results will also be considered.

REFERENCES

[1] H. Mazdarani, B. Sainsbury, J. Watterson, R. Hibbert, and C. Rossa, "Ultrasound-based visual servoing for out-of-plane longitudinal needle tracking in robot-aided percutaneous nephrolithotomy," *IEEE Access*, vol. 13, pp. 69 090–69 102, 2025.

[2] G. Reusz, P. Sarkany, J. Gal, and A. Csomos, "Needle-related ultrasound artifacts and their importance in anaesthetic practice," *British Journal of Anaesthesia*, vol. 112, no. 5, pp. 794–802, 2014.

[3] G. Penney *et al.*, "Registration of freehand 3D ultrasound and magnetic resonance liver images," *Medical Image Analysis*, vol. 8, no. 1, pp. 81–91, 2004.

[4] B. Hou *et al.*, "Predicting slice-to-volume transformation in presence of arbitrary subject motion," in *Medical Image Computing and Computer-Assisted Intervention Conference*, 2017, pp. 296–304.

[5] Y. Velikova, M. Azampour, W. Simson, M. Esposito, and N. Navab, "Implicit neural representations for breathing-compensated volume reconstruction in robotic ultrasound," in *Inter. Conference on Robotics and Automation*, 2024, pp. 1316–1322.

[6] A. Gee *et al.*, "Sensorless freehand 3D ultrasound in real tissue: Speckle decorrelation without fully developed speckle," *Medical Image Analysis*, vol. 10, no. 2, pp. 137–149, 2006.

[7] H. Kim and T. Varghese, "Hybrid spectral domain method for attenuation slope estimation," *Ultrasound in Medicine & Biology*, vol. 34, no. 11, pp. 1808–1819, 2008.

[8] P. Hellier, P. Coupé, X. Morandi, and D. L. Collins, "An automatic geometrical and statistical method to detect acoustic shadows in intraoperative ultrasound brain images," *Medical Image Analysis*, vol. 14, no. 2, pp. 195–204, 2010.

[9] A. Broersen *et al.*, "Enhanced characterization of calcified areas in intravascular ultrasound virtual histology images by quantification of the acoustic shadow: validation against computed tomography coronary angiography," *The Inter. Journal of Cardiovascular Imaging*, vol. 32, pp. 543–552, 2016.

[10] F. Berton, F. Cheriet, M.-C. Miron, and C. Laporte, "Segmentation of the spinous process and its acoustic shadow in vertebral ultrasound images," *Computers in Biology and Medicine*, vol. 72, pp. 201–211, 2016.

[11] X. Chen *et al.*, "A freehand 3D ultrasound reconstruction method based on deep learning," *Electronics*, vol. 12, no. 7, p. 1527, 2023.

[12] Q. Zou *et al.*, "3D ultrasound image reconstruction based on 3D-resnet in the musculoskeletal system using a 1d probe: ex vivo and in vivo feasibility studies," *Physics in Medicine & Biology*, vol. 68, no. 16, p. 165003, 2023.

[13] C.-H. Lin, Y.-N. Sun, and C.-J. Lin, "A motion compounding technique for speckle reduction in ultrasound images," *Journal of Digital Imaging*, vol. 23, pp. 246–257, 2010.

[14] R. Rohling, A. Gee, and L. Berman, "Three-dimensional spatial compounding of ultrasound images," *Medical Image Analysis*, vol. 1, no. 3, pp. 177–193, 1997.

[15] D. F. Leotta and R. W. Martin, "Three-dimensional spatial compounding of ultrasound scans with weighting by incidence angle," *Ultrasonic Imaging*, vol. 22, no. 1, pp. 1–19, 2000.

[16] V. Grau and J. A. Noble, "Adaptive multiscale ultrasound compounding using phase information," in *Conf. on Information Processing in Computer-Assisted Interventions*, 2005, pp. 589–596.

[17] C. Yao *et al.*, "Multi-view 3D echocardiography compounding based on feature consistency," *Physics in Medicine & Biology*, vol. 56, no. 18, p. 6109, 2011.

[18] Y. Lu *et al.*, "Free scan real time 3D ultrasound imaging with shading artefacts removal," *Ultrasonics*, vol. 135, p. 107091, 2023.

[19] J. Perez-Gonzalez *et al.*, "Spatial compounding of 3-d fetal brain ultrasound using probabilistic maps," *Ultrasound in Medicine & Biology*, vol. 44, no. 1, pp. 278–291, 2018.

[20] J. Perez-Gonzalez, N. Hevia Montiel, and V. M. Bañuelos, "Deep learning spatial compounding from multiple fetal head ultrasound acquisitions," in *Medical Ultrasound, and Preterm, Perinatal and Paediatric Image Analysis Workshop*, 2020, pp. 305–314.

[21] R. Wright *et al.*, "Fast fetal head compounding from multi-view 3d ultrasound," *Medical Image Analysis*, vol. 89, p. 102793, 2023.

[22] A. Karamalis *et al.*, "Ultrasound confidence maps using random walks," vol. 16, no. 6, pp. 1101–1112, 2012.

[23] A. L. Y. Hung, W. Chen, and J. Galeotti, "Ultrasound confidence maps of intensity and structure based on directed acyclic graphs and artifact models," in *Inter. Symp. on Biomedical Imaging*, 2021, pp. 697–701.

[24] Q. Meng *et al.*, "Weakly supervised estimation of shadow confidence maps in fetal ultrasound imaging," *Transactions on Medical Imaging*, vol. 38, no. 12, pp. 2755–2767, 2019.

[25] C. S. Berge, A. Kapoor, and N. Navab, "Orientation-driven ultrasound compounding using uncertainty information," in *Conf. on Information Processing in Computer-Assisted Interventions*, 2014, pp. 236–245.

[26] H. Mazdarani, A. Cotton, and C. Rossa, "2d ultrasound-guided visual servoing for in-plane needle tracking in robot-assisted percutaneous nephrolithotomy," in *Inter. Conference on Systems, Man, and Cybernetics*, 2023, pp. 1786–1791.

[27] F. Mohamed and C. V. Siang, "A survey on 3D ultrasound reconstruction techniques," *Artificial Intelligence - Applications in Medicine and Biology*, pp. 73–92, 2019.